PHYSICAL REVIEW B **107**, 085149 (2023)

Tuning scintillation properties of Lu_2SiO_5 by Ce and Ca codoping

Jiajia Cai [1,*] and Yau-yuen Yeung [2,†]
[1] *College of Electrical Engineering, Henan University of Technology, Zhengzhou 450001, China*
[2] *Department of Science and Environmental Studies, The Education University of Hong Kong,*
10 Lo Ping Road, Tai Po, N.T., Hong Kong, China

(Received 25 October 2022; revised 6 February 2023; accepted 15 February 2023; published 27 February 2023)

The light-yield enhancement and decay-time shortening by Ca codoped with Lu_2SiO_5:Ce have been observed in experiment. However, the underlying mechanisms remain enigmatic. First-principles calculations are performed to gain insight into the effect of Ca codoping. We show that first, the formation of Ca_{Lu}-V_O complex defects is favored, which causes the dissociation of Ce_{Lu}-V_O; therefore, the nonradiative decay of Ce via V_O is suppressed, leading to light-yield enhancement. Secondly, the downward shift of the Fermi level by the codoping effect causes the observation of Ce^{4+} ions, and the electron trap depth of V_O decreases by the combination with Ca; thus, the trapping/detrapping rates increase, leading to decay-time shortening. Hence, our study has demonstrated an effective way to gain insight into the mechanisms for tuning properties of optical materials by codoping. The principles of the obtained mechanisms provide guidance for designing and optimizing a broad range of functional materials.

DOI: 10.1103/PhysRevB.107.085149

I. INTRODUCTION

Cerium-doped Lu_2SiO_5:Ce (LSO:Ce) has drawn considerable attention due to its appealing properties for scintillator applications in positron emission tomography [1]. It is noted that codoping such as Li/Ca/Mg/Cu/Tb/Dy/Yb contributes to the improvement of the scintillation properties of LSO:Ce [2–9]. In particular, it is experimentally proposed that codoping with divalent Ca^{2+} ions significantly enhances the light yield and shortens the decay time of LSO:Ce, which are attributed to the suppression of electron trapping and the formation of stable Ce^{4+} ions, respectively [3,9]. However, it is observed that the scintillation properties of LSO:Ce show essentially different variations with Li codoping concentration increasing [5]. Though the effects of codoping on the scintillation properties of LSO:Ce have been observed, challenges center around the understanding of the underlying mechanisms, especially the elucidation of the above correlations: (1) Ca codoping → electron traps suppression → light yield enhancement; (2) Ca codoping → emergence of stable Ce^{4+} ions → scintillation decay-time shortening.

Actually, the light-yield performance of many optical materials is limited by nonradiative decay processes commonly including thermal quenching and charge transfer via phonons and defects, respectively. And, the charge-state transition of a certain defect is typically attributed to the Fermi-energy shifting, which is possibly caused by the codoping and/or the annealing. Thus, to understand the codoping effect on scintillation properties, it is essential to determine the defects introduced, their charge states, and trap levels so as to analyze their impacts on the nonradiative decay processes and Fermi level in the sample. The mechanisms revealed in this work are expected to shed light on design and optimization in a broad range of functional materials for applications in various fields including optical and thermoelectric materials, semiconductor, and magnetic devices.

In the present work, first-principles calculations based on density-functional theory (DFT), which usually yield reliable information about not only the energy but also the atomic coordinate of the defect [10,11], are performed on LSO:Ce, Ca. Considering that a considerable amount of oxygen vacancies V_O act as deep electron traps [12], we will discuss not only the formation of isolated defects but also the effect of Ca codoping on the V_O-involved complex defects. As the hybrid DFT (HDFT) approach in the framework of generalized Kohn-Sham (GKS) theory can be utilized to obtain a more reasonable energy-level structure than that in Kohn-Sham (KS) scheme [13], the luminescence properties of LSO:Ce are evaluated based on the GKS eigenvalues of the valence-band maximum (VBM), the conduction-band minimum (CBM), and the $4f$ and $5d$ orbitals. Simulations on the charge-transfer process between Ce and V_O are carried out to disclose the role of Ca on the light-yield improvement of LSO:Ce, Ca. Moreover, the Ca codoping effect on the Fermi level is quantified to understand the observation of stable Ce^{4+} ions, and the relative positions of $5d$ and CBM are obtained to unravel the role of Ce^{4+} on scintillation decay-time shortening.

II. COMPUTATIONAL METHODOLOGY

The first-principles calculations based on DFT within generalized gradient approximation (GGA) using the Perdew-Burke-Ernzerhof (PBE) exchange-correlation functional are adopted for atomic relaxation, as implemented in the

---

[*] Corresponding author: jjcai@mail.ustc.edu.cn

[†] Corresponding author: dr.yeung@physics.org

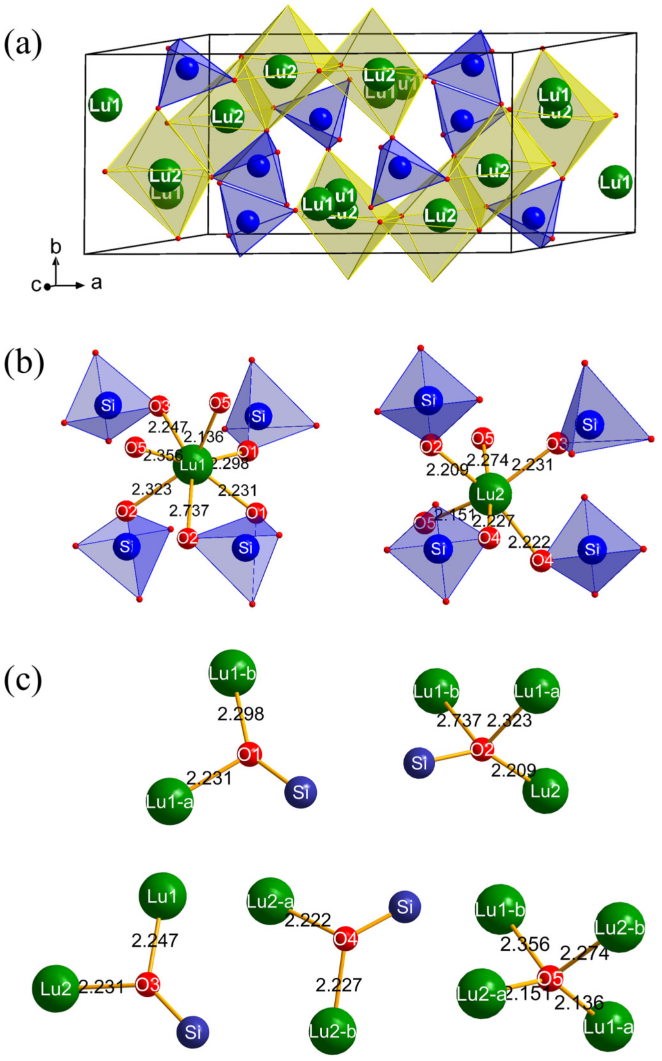

FIG. 1. (a) Crystal structure of Lu_2SiO_5, and the local structure of the two Lu sites (b) and five oxygen sites (c) in Lu_2SiO_5. The marked Lu–O bond lengths are in angstrom (Å). The seven-coordinated Lu is denoted as Lu1 and the six-coordinated Lu is denoted as Lu2. For the O sites, if the O atom has two coordinated Lu1 (or Lu2) atoms, the Lu1 (or Lu2) atom with a shorter Lu–O bond length is labeled "a," and the other with a longer Lu–O bond length is labeled "b."

Vienna *Ab initio* Simulation Package (VASP) [14–18]. The Lu ($5p^6$ $5d^1$ $6s^2$), Si ($3s^2$ $3p^2$), O ($2s^2$ $2p^4$), Ce ($5s^2$ $5p^6$ $4f^1$ $5d^1$ $6s^2$), and Ca ($3p^6$ $4s^2$) are treated as valence electrons. The interactions between valence electrons with the cores are described by the projector augmented-wave method [19]. The total energy threshold is 10^{-6} eV and the Hellmann-Feynman force threshold is 0.01 eV/Å. The plane-wave cutoff energy is set to 400 eV. For sampling the Brillouin zone, $1 \times 3 \times 1$ k points centered at the Γ point are used for the unit cell. A supercell composed of $1 \times 2 \times 1$ unit cells is chosen to model various defects as a compromise between computational cost and accuracy, and only one k-point Γ is used for the $1 \times 2 \times 1$ supercell.

As shown in Fig. 1(a), the unit cell of Lu_2SiO_5 (LSO) contains 64 atoms. The experimentally measured lattice parameters of LSO are $\alpha = \gamma = 90^\circ$, $\beta = 122.22^\circ$, $a = 14.28$ Å, $b = 6.64$ Å, and $c = 10.25$ Å [20], and the corresponding DFT-optimized values are $\alpha = \gamma = 90^\circ$, $\beta = 121.95^\circ$, $a = 14.28$ Å, $b = 6.67$ Å, and $c = 10.28$ Å. The theoretical results of the pure-crystal lattice parameters are consistent with the experimental values, within 0.5% relative difference. Fractional atomic coordinates of LSO in experiment [20] and from our GGA-PBE calculations are provided in Table S1 of Supplemental Material [21]. There are two Lu sites, one Si site, and five oxygen sites in LSO, and the naming of the Lu and O sites is indicated in Figs. 1(b) and 1(c). Detailed geometric parameters of LSO are listed in Table S2 [21].

The band structure and density of states (DOSs) are calculated and plotted in Fig. 2. It is indicated that the LSO is a direct-gap material with a $\Gamma \rightarrow \Gamma$ direct band gap of 4.67 eV from our GGA-PBE calculations. As is well known, the band gaps are substantially underestimated by GGA-type functionals. The HDFT calculations are performed to overcome the underestimation of the band gap by the standard DFT calculations. There is an almost linear correlation between the optimized Hartree-Fock (HF) mixing α parameter (by setting the screen parameter $\mu = 0$) and the inverse of the high-frequency dielectric constant $1/\varepsilon_\infty$ [22–24]; thus, the modified PBE0 with $\alpha = 0.29$ is adopted ($\varepsilon_\infty \approx 3.4$ for LSO based on our dielectric constant calculation) to obtain the improved electronic structure. The $\Gamma \rightarrow \Gamma$ direct band gap of LSO is calculated to be 7.40 eV from HDFT-PBE0 calculation. Moreover, as indicated in Fig. 2, the projected DOSs show that the dominant components of the valence band-edge states are O-$2p$ orbitals, while the dominant components of the conduction band-edge states are Lu-$5d$ orbitals. In experiment, a sharp exciton band originating from O-$2p \rightarrow$ Lu-$5d$ transition is observed at 7.27 eV at 6 K, with the fundamental band-gap energy of 7.52 eV [25]. It is concluded that the fundamental gap is substantially underestimated by GGA-PBE functionals, while our obtained GKS gap (7.40 eV) provides a reasonable estimation on the fundamental gap.

The difficulty of formation of a defect X^q (q being the net charge) increases sharply with its formation energy calculated as follows [26]:

$$E^f(X^q) = [E_{\rm tot}(X^q) + E_{\rm corr}(X^q) + q\Delta V_{\rm NAP}] - \left[E_{\rm tot}({\rm bulk}) + \sum_i n_i\mu_i - qE_F\right]. \qquad (1)$$

$E_{\rm tot}(X^q)$ and $E_{\rm tot}({\rm bulk})$ are the total energies of the supercell containing defect X^q and the equivalent supercell of perfect crystal, respectively. n_i is the change in the number of atom i, and μ_i is the chemical potential of atom i. The chemical potential of the electron is the Fermi energy E_F. The ranges of chemical potentials are restricted by the depletion of Lu_2O_3, SiO_2, and CeO_2, and the stable region of LSO formation for chemical potential ranges of O and Si is determined by referring to Ref. [27] (for details see Part S1.2 of Supplemental Material [21]). As a result, $\Delta\mu(O) = -5.0$ eV in O-poor limit, and $\Delta\mu(O) = -1.5$ eV in O-rich limit are determined. μ(Ce) is determined by fixing the calculated total concentrations of Ce (assuming 1.0 mol. % relative to LSO in this work). The equilibrium Fermi level

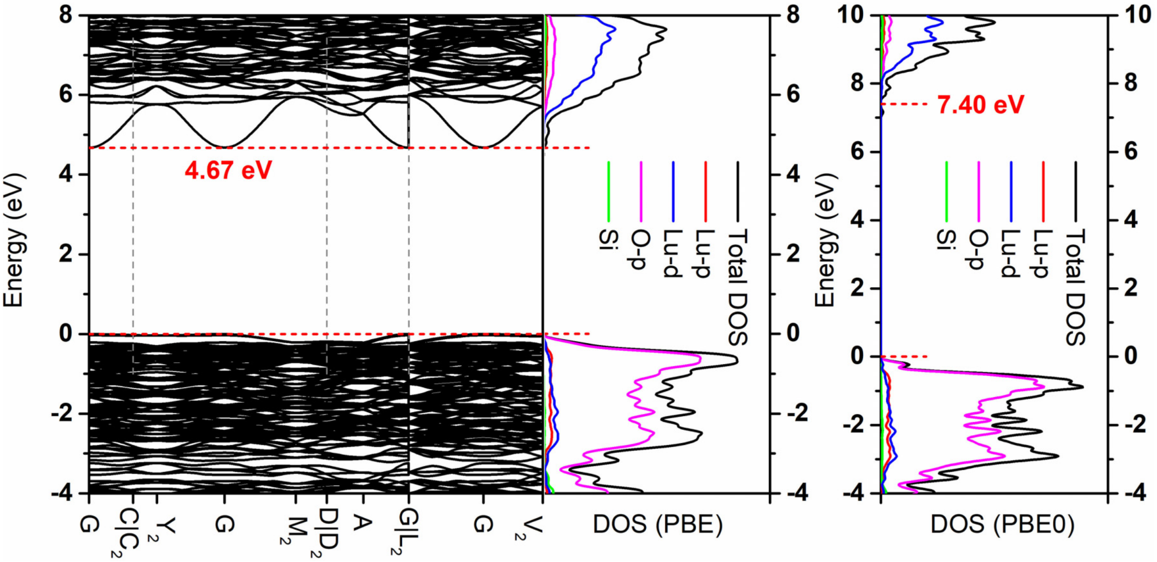

FIG. 2. Band structure and density of states of Lu_2SiO_5. The energy zeros are set at the VBM. The $\Gamma \rightarrow \Gamma$ direct band gap of Lu_2SiO_5 is calculated to be 4.67 and 7.40 eV, respectively, from GGA-PBE and HDFT-PBE0 calculations. Dominant components of the valence band-edge states are O-2p orbitals, while the dominant components of the conduction band-edge states are Lu-5d orbitals.

$E_F^{(\mathrm{eq})}$ is determined by charge neutrality. To account for the finite-size effects, the obtained association energy can be corrected by the widely available correction method by Frysoldt, Neugebauer, and van de Walle and developed by Kumagai [28,29]. As an alternative correction scheme, the detail-insensitive imagine-charge (IC) correction E_{corr} of Lany and Zunger [30] (a modified version of the Makov-Payne correction [31,32]) combined with simplified potential alignment (PA) correction $q\Delta V_{\mathrm{NAP}}$ by Durrant *et al.* [33] (in which the NAP stands for the neglect of the average electrostatic potential) is adopted as a compromise of computational accuracy and simplicity in this work. As a result, E_{corr} is calculated to be about 0.14 q^2 eV, and ΔV_{NAP} is calculated to be −0.06 eV for V_{O}, −0.17 eV for V_{Lu}, −0.15 eV for V_{Si}, 0.13 eV for $\mathrm{Ce_{Lu}}$, 0.15 eV for $\mathrm{Ce_{Si}}$, and 0.03 eV for $\mathrm{Ca_{Lu}}$. By referring to the formation energy convergence check method by Kumagai *et al.* [34], the defect-formation energy errors by adopting the correction scheme on 1 × 2 × 1 supercells are expected to be less than 0.32 eV. Actually, in this work, what we are concerned with are the corrections on V_{O1} and $\mathrm{Ce_{Lu1}}$, and it is found that the formation energy errors of the singly and doubly charged defects by adopting 1 × 2 × 1 supercells are expected to be less than 0.04 eV. To sum up, the small defect-formation energy errors support the validity of our adoption of the correction scheme on the 1 × 2 × 1 supercells. For details of the aforementioned IC and PA corrections and the formation energy error caused by the finite size of supercell, see Part S1.3 of Supplemental Material [21].

As intrinsic defects, vacancies of Lu, Si, and O, interstitials of O, and antisites of $\mathrm{Lu_{Si}}$ and $\mathrm{Si_{Lu}}$ are taken into account in our simulations. Considering that the Lu and Si are situated in the polyhedra of O, the formation of the interstitials of Lu and Si is expected to be unfavored, thus ignored in our simulations. Among numerous possible original configurations of oxygen interstitials, the configurations in which the O atoms situate at the middle of two nearest Lu1-Lu1, Lu2-Lu2, Lu1-Lu2, Lu1-Si, Lu2-Si, and Si-Si are simulated in this work. Antisites of $\mathrm{Lu_O}$ are not taken into account in view of that the valence states of Lu and O ions differ greatly. And, we perform calculations on $\mathrm{Ce_{Lu}}$, $\mathrm{Ca_{Lu}}$, $\mathrm{Ce_{Si}}$, and $\mathrm{Ca_{Si}}$ to evaluate the site-occupancy preference of Ce and Ca in LSO. For Ce-doped supercells, a Hubbard U (4-eV) term was added in PBE calculations empirically for better treatment of the 4f states [35].

If the defect reaches thermodynamic equilibrium distribution at temperature T, its concentration can be related to the formation energy as an approximation to Gibbs energy of formation with the following expression:

$$C = N_{\mathrm{site}} N_{\mathrm{config}} \exp(-E^f/kT). \tag{2}$$

Here, N_{site} is the number of Lu sites in LSO where Ce can be incorporated. N_{config} describes possible additional degeneracies, which is on the order of unit and ignored. E^f is the calculated formation energy as an approximation of the Gibbs formation energy. We assume full equilibrium of LSO:Ce at a temperature of about 1400 °C ($kT \sim 0.14$ eV) by referring to the experimental sintering temperatures [36,37].

III. RESULTS AND DISCUSSION

A. Defect formation preference and charge transition level

Under O-poor limit $\Delta\mu(O) = -5.0$ eV, which is close to the LSO crystal-growth conditions, the formation energies of the intrinsic vacancies indicate that V_{Lu} and V_{Si} defects are hardly formed due to high formation energies, while a considerable amount of V_{O}, which are actually in the positively charged states, act as deep electron traps and delay the recombination of electron-hole pairs at the luminescence centers, resulting in room-temperature afterglow and thereby reducing the light yield [12]. Moreover, it is found that the most stable oxygen interstitial I_{O} is the one in which the O atom originally

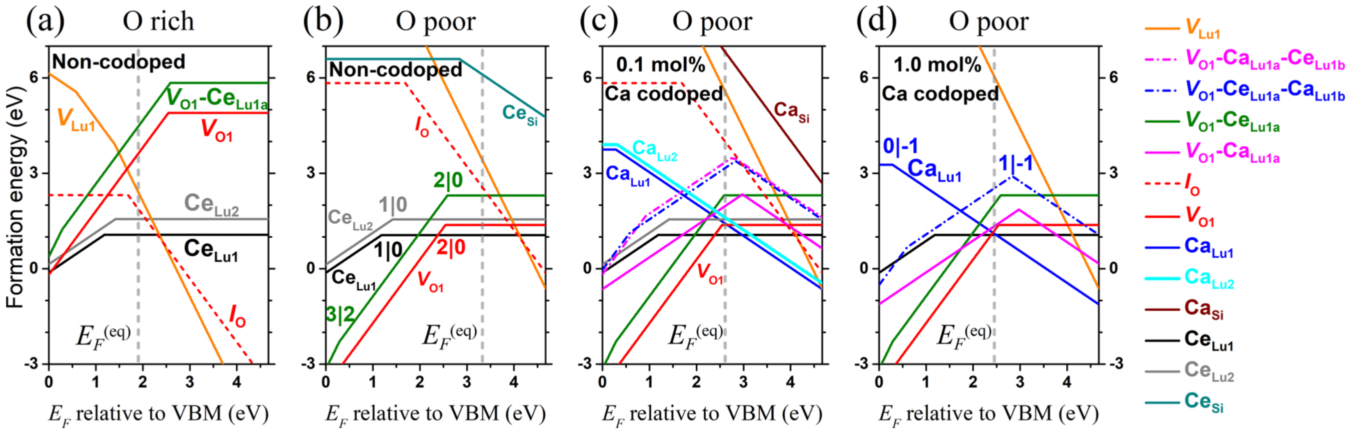

FIG. 3. Formation energies of defects as a function of E_F in LSO:Ce under chemical potential conditions of O-rich limit $\Delta\mu(\mathrm{O}) = -1.5$ eV (a) and O-poor limit $\Delta\mu(\mathrm{O}) = -5.0$ eV (b), and formation energies of defects as a function of E_F in 0.1 mol. % Ca codoped (c) and 1.0 mol. % Ca codoped (d). LSO:Ce under O-poor limit $\Delta\mu(\mathrm{O}) = -5.0$ eV. Concentrations of Ce are fixed at 1.0 mol%. With both the increase in oxygen and the codoping of Ca, the $E_F^{(eq)}$ shifts sharply down, leading to the emergence of stable Ce^{4+} ions in LSO:Ce. With the increase of Ca codoping concentration, the formation energy of +1-charged V_{O1}-$\mathrm{Ca}_{\mathrm{Lu1a}}$ becomes further lower than that of +2-charged V_{O1}-$\mathrm{Ce}_{\mathrm{Lu1a}}$ at $E_F^{(eq)}$; the formation of $\mathrm{Ca}_{\mathrm{Lu}}$-$V_{\mathrm{O}}$ complex defects, therefore, causes the dissociation of spatial-correlated V_{O} and $\mathrm{Ce}_{\mathrm{Lu}}$.

situates at the middle of the nearest Lu2-Si among various possible configurations. The formation energies ordered from low to high at $E_F^{(eq)}$ are the neutral $V_{\mathrm{O1}}^{\times}$, $V_{\mathrm{O4}}^{\times}$, $V_{\mathrm{O3}}^{\times}$, $V_{\mathrm{O2}}^{\times}$, and $V_{\mathrm{O5}}^{\times}$ and the doubly charged I''_{O} (in the aforementioned most stable configuration), then the neutral $\mathrm{Si}_{\mathrm{Lu1}}^{\times}$, the singly charged $\mathrm{Si}_{\mathrm{Lu2}}^{\cdot}$ and $\mathrm{Lu}'_{\mathrm{Si}}$, the triply charged V_{Lu1}''' and V_{Lu2}''', and finally the quadruply charged V_{Si}''''. Besides, it is noted that the most stable doubly charged oxygen vacancy is $V_{\mathrm{O1}}^{\cdot\cdot}$. More details are provided in Fig. S4 and Table S3 of Supplemental Material [21].

As the formation energy curves indicated in Fig. 3(b), Ce prefers to occupy the seven-coordinated Lu1 site over the six-coordinated Lu2 site, and the four-coordinated $\mathrm{Ce}_{\mathrm{Si}}$ defects are unlikely to form. In particular, it is found that the $\mathrm{Ce}_{\mathrm{Lu1}}^{\times}$ defect has a lower formation energy of 0.49 eV than the $\mathrm{Ce}_{\mathrm{Lu2}}^{\times}$. It is noted that the average length of the seven-coordinated Lu-O bonds of Lu1 (2.33 Å) is about 0.1 Å larger than that of the six-coordinated Lu-O bonds of Lu2 (2.22 Å), and the average length of the four-coordinated Si-O bonds is 1.65 Å. And, the effective ionic radii both of the seven-coordinated Ce^{3+}(1.07 Å) and the six-coordinated Ce^{3+}(1.01 Å) are about 0.1 Å larger than those of Lu^{3+} (about 0.9 Å) [38]. Therefore, Ce^{3+} ions in LSO prefer to occupy the less compact Lu1 site over the Lu2 site. While the effective ionic radius of the four-coordinated Si^{4+}(0.26 Å) is much smaller than that of Ce^{3+} (about 1 Å), thus the occupancy of Ce^{3+} at Si site is negligible. Our assessment is consistent with previous experimental observations and theoretical studies [35,39–41]. It is foreseeable that the codopants Ca show similar site-occupancy preference with the dopants Ce, as the effective ionic radii of both the seven-coordinated Ca^{2+} (1.06 Å) and the six-coordinated Ca^{2+} (1.01 Å) are close to those of Ce^{3+}. As a result, in the case of 0.1 mol. % Ca and 1 mol. % Ce-codoped LSO under O-poor limit, as indicated in Fig. 3(c), Ca also prefers to occupy the seven-coordinated Lu1 site over the six-coordinated Lu2 site, and the four-coordinated $\mathrm{Ca}_{\mathrm{Si}}$ defects are unlikely to form. And, it is found that the $\mathrm{Ca}'_{\mathrm{Lu1}}$ defect has a lower formation energy (0.19 eV) than $\mathrm{Ca}'_{\mathrm{Lu2}}$.

The combination of the oxygen interstitial makes the polyhedra of Lu1-O more compact (Table S4 [21]); it is therefore expected that the dopant Ce and codopant Ca atoms tend not to occupy the Lu sites accompanied by a nearby oxygen interstitial. Besides, it is noted that the $\mathrm{Ce}_{\mathrm{Lu}}$ (or $\mathrm{Ca}_{\mathrm{Lu}}$) can combine with oxygen vacancy to form 13 different V_{O}-$\mathrm{Ce}_{\mathrm{Lu}}$ (or V_{O}-$\mathrm{Ca}_{\mathrm{Lu}}$) complex defects; see Fig. 1(c). It is indicated from the relative formation energy of the isomeric V_{O}-involved complex defects in LSO:Ce (Table S5 [21]) that the stable V_{O}-$\mathrm{Ce}_{\mathrm{Lu}}$-type complex defect in $+2/+1/0$ charge state is V_{O1}-$\mathrm{Ce}_{\mathrm{Lu1a}}$, and the stable V_{O}-$\mathrm{Ca}_{\mathrm{Lu}}$-type complex defect in $+2/+1/0/-1$ charge state is V_{O1}-$\mathrm{Ca}_{\mathrm{Lu1a}}$.

We define the binding energy of a complex defect as the formation energy of the complex defect minus the sum of the formation energies of its constituent defects. Obviously, the lower binding energy (formation energy) indicates the more stable complex defect. Besides, the valence of Ce in the complex defects can be obtained by examining the occupation of the $4f$ and $5d$ orbitals. As a result, the binding energies of the $-2/-3$ charged I_{O}-$\mathrm{Ce}_{\mathrm{Lu1}}$ complex defects relative to the $-2/-3$ charged I_{O} (in the configuration in which the O atom originally situates at the middle of two nearest Lu1-Si) and neutral $\mathrm{Ce}_{\mathrm{Lu1}}$ are 0.11/0.13 eV. And, it is noted that the valence of Ce in the $0/-1$ charged I_{O}-$\mathrm{Ce}_{\mathrm{Lu1}}$ complex defects are +4. Thus, it is confirmed that the $\mathrm{Ce}_{\mathrm{Lu1}}^{\times}$ defect tends not to combine with the oxygen interstitials. The binding energy of the dominant V_{O}-involved complex defects (Table S6 [21]), including V_{O}-$\mathrm{Ce}_{\mathrm{Lu}}$, V_{O}-$\mathrm{Ca}_{\mathrm{Lu}}$, and V_{O}-$\mathrm{Ca}_{\mathrm{Lu}}$-$\mathrm{Ce}_{\mathrm{Lu}}$, indicates that the $\mathrm{Ce}_{\mathrm{Lu}}$ dopants tend to combine the V_{O} defects, especially the positively charged V_{O}, and $\mathrm{Ca}_{\mathrm{Lu}}$ combines the charged V_{O} defects more strongly than $\mathrm{Ce}_{\mathrm{Lu}}$, while the formation of V_{O}-$\mathrm{Ca}_{\mathrm{Lu}}$-$\mathrm{Ce}_{\mathrm{Lu}}$-type triple-complex defects is definitely unfavorable. Thus, the formation of $\mathrm{Ca}_{\mathrm{Lu}}$-$V_{\mathrm{O}}$ complex defects tends to dissociate the originally spatial-correlated V_{O} and $\mathrm{Ce}_{\mathrm{Lu}}$.

The charge-transition level (CTL) $\varepsilon(q_1/q_2)$, which is defined as the Fermi energy E_F at which the formation energies of the defects containing defect X_1^q and containing X_2^q are equal, is calculated by utilizing the expression [26]

$$\varepsilon(q_1/q_2) = \frac{E_{\mathrm{tot}}(X^{q_1}) - E_{\mathrm{tot}}(X^{q_2})}{q_2 - q_1}. \tag{3}$$

Figure 3 shows the formation energies of the dominant isolated and complex defects as a function of E_F. The CTL can be identified with the crossover point in plots of the formation energies of defects at different charge states. From the formation energy curve of $\mathrm{Ce^{3+}/Ce^{4+}}$ under O-poor limit in Fig. 3(b), it is indicated that the CTL $\varepsilon(0/+1)$ of both $\mathrm{Ce_{Lu1}}$ and $\mathrm{Ce_{Lu2}}$ defects are far below the $E_F^{(\mathrm{eq})}$; thus, stable $\mathrm{Ce^{4+}}$ ions can be deduced to be inexistent in noncodoped LSO:Ce, in good agreement with the experimental observation that LSO:Ce single crystals contain only $\mathrm{Ce^{3+}}$ ions [42].

As indicated in Figs. 3(c) and 3(d), the formation energy curves of the defects including $\mathrm{Ca_{Lu}}$ shift sharply down with the increase of Ca codoping concentration. Especially, the formation energy of +1-charged V_{O1}-$\mathrm{Ca_{Lu1a}}$ becomes further lower than that of +2-charged V_{O1}-$\mathrm{Ce_{Lu1a}}$ at $E_F^{(\mathrm{eq})}$. It is noteworthy that, due to the aliovalent codoping effect [43] by the introduction of Ca, the $E_F^{(\mathrm{eq})}$ shifts downward by 1 eV or more; thus, the formation probability of the locally +1-charged $\mathrm{Ce^{4+}}$ is promoted. Therefore, the experimental observation that stable $\mathrm{Ce^{4+}}$ gets enriched with Ca codoping [4] can be well understood.

As indicated in the leftmost part of Fig. 3(a), in the case of O rich, the formation energy curves of the V_{O}-included defects would shift up, the formation energy curve of I_{O} would shift down, and $E_F^{(\mathrm{eq})}$ would shift down by about 1.4 eV compared to the case of O poor. In practice, the case of O rich corresponds to the air-atmosphere annealing on LSO:Ce crystal. Oxygen vacancies generally act as deep electron traps, while the oxygen vacancies are not favored after air annealing; thus, the experimental observation that air annealing on LSO:Ce contributes to the reduction in the content of deep traps (possibly including oxygen vacancy) [44], can be interpreted. Besides, as the downshift of $E_F^{(\mathrm{eq})}$ promotes the formation probability of high charge-state ions such as $\mathrm{Ce^{4+}}$, thus the emergence of stable $\mathrm{Ce^{4+}}$ is observed by air-atmosphere annealing [44].

To quantify the relative positions of CTL $\varepsilon(q_1/q_2)$ of various defects in the host band gap, the KS eigenvalue of the VBM and the CBM are chosen as references in our GGA-PBE calculations. The fundamental gap of LSO is 4.67 eV from GGA-PBE calculation. The positions of $\varepsilon(q_1/q_2)$ in the gap (detailed data provided in Table S7 [21]) are plotted in Fig. 4. It is indicated that V_{O1} provides deep CTL $\varepsilon(0/+2)$ with a trap depth of 2.13 eV below the CBM, in consistence with the assessment that V_{O} commonly features deep CTLs in wide band-gap oxides [45]. V_{Lu1} provides CTLs $\varepsilon(-1/0)$, $\varepsilon(-2/-1)$, and $\varepsilon(-3/-2)$ in the gap. The $\mathrm{Ce_{Lu1}}$ and $\mathrm{Ce_{Lu2}}$ defects introduce CTL $\varepsilon(0/+1)$ with trap depths, respectively, of 1.19 and 1.42 eV above the VBM. And, the $\mathrm{Ca_{Lu1}}$ defect introduces CTL $\varepsilon(-1/0)$ with a trap depth of 0.29 eV above the VBM. It is noted that the CTLs $\varepsilon(0/+2)$ of V_{O1}-$\mathrm{Ce_{Lu1a}}$, $\varepsilon(-1/+1)$ of V_{O1}-$\mathrm{Ca_{Lu1a}}$, and $\varepsilon(-1/+1)$ of V_{O1}-$\mathrm{Ca_{Lu1a}}$-$\mathrm{Ce_{Lu1b}}$ and V_{O1}-$\mathrm{Ce_{Lu1a}}$-$\mathrm{Ca_{Lu1b}}$, respectively, with trap depths of 2.08, 1.69, 1.89, and 1.84 eV below the CBM, are possibly related to the $\varepsilon(0/+2)$ of V_{O1} defect. It is implied that the combination of $\mathrm{Ce_{Lu1}}$ with V_{O1} shows little effect on the position of the CTL $\varepsilon(0/+2)$ of V_{O1}, while the combination of $\mathrm{Ca_{Lu1}}$ with V_{O1} shifts $\varepsilon(0/+2)$ of V_{O1} closer to the CBM by up to 0.44 eV, which contributes to the faster trapping/detrapping rates, leading to scintillation decay-time shortening of LSO:Ce. Besides, both the $\varepsilon(+2/+3)$ of V_{O1}-$\mathrm{Ce_{Lu1a}}$ and $\varepsilon(+1/+2)$ of V_{O1}-$\mathrm{Ca_{Lu1a}}$-$\mathrm{Ce_{Lu1b}}$ (or V_{O1}-$\mathrm{Ce_{Lu1a}}$-$\mathrm{Ca_{Lu1b}}$) are related to the charge transition between $\mathrm{Ce^{3+}}$ and $\mathrm{Ce^{4+}}$. Compared to $\varepsilon(0/+1)$ of isolated $\mathrm{Ce_{Lu1}}$ defect, the combination of V_{O1} with $\mathrm{Ce_{Lu1}}$ dramatically decreases $\varepsilon(\mathrm{Ce^{3+}/Ce^{4+}})$-VBM, while the further combination of $\mathrm{Ca_{Lu1}}$ with V_{O1}-$\mathrm{Ce_{Lu1}}$ effectively weakens the decrease. HDFT calculations are performed to overcome the underestimation of the band gap by the standard DFT calculations. It is indicated from the CTL data (Table S7 [21]) that the HDFT-PBE0 calculation results are reasonably consistent with the GGA-PBE calculation results considering the accuracy of the models and errors in each component.

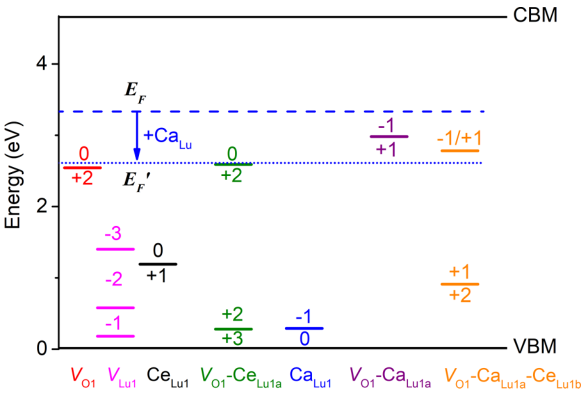

FIG. 4. Charge-transition level of defects relative to the host band edges in LSO:Ce, Ca from GGA-PBE calculations. The downward shift of $E_F^{(\mathrm{eq})}$ with the codoping of 0.1 mol. % Ca causes the observation of stable $\mathrm{Ce^{4+}}$ ions, and the combination with Ca decreases the electron trap depth of V_{O}; both the two processes contribute to the faster trapping/detrapping rates.

B. Luminescence properties

As the band gaps are substantially underestimated by the traditional workhorse of DFT, which leads to the underestimation of the CBM, our GGA-PBE calculations to determine the excited $(\mathrm{Ce^{3+}})^*$ state by constrained-occupancy approach through setting the energy-ordered occupation numbers fail to place the lowest $5d$ orbital below the CBM. In this work, constrained-occupancy HDFT calculations are performed to obtain the equilibrium configuration of the excited $(\mathrm{Ce^{3+}})^*$ state. For details on constrained-occupancy approach, see Ref. [46]. The energy difference between the unoccupied lowest $5d$ orbital and the predominantly CBM orbital (with one electron removed from the $\mathrm{Ce^{3+}}$-doped supercell) in the GKS framework can be defined as the energy required by the electron of the $\mathrm{Ce^{3+}}$ impurity at a lowest excited state of $5d$ character through vertical ionization to the CBM, and the energy difference between the unoccupied $4f$ and $5d$ orbitals in the GKS framework can be used to estimate the excitation and emission energies under the corresponding equilibrium geometric structures following the Franck-Condon principle [47]. Considering that the Ce^{3+} ion has one electron in the $4f$ shell, and the emission is based on the electronic transition from the lowest $5d$ energy level to two $4f$ ground levels ($^2F_{5/2}$ and $^2F_{7/2}$), which have an energy separation of typically $\sim 2200\,cm^{-1}$ from the spin-orbit interaction, spin-orbit interaction is not included self-consistently in this work but rather added as a perturbation to the $4f$ states for optical transitions, which is estimated to be a blueshift of about $2\zeta_{4f} = 0.15$ eV by adopting $\zeta_{4f} \approx 615\,cm^{-1}$ [48]. With the impact of spin-orbit interaction involved, the excitation and emission energies are calculated to be, respectively, 4.01 and 3.72 eV for Ce_{Lu1}, and 3.89 and 3.16 eV for Ce_{Lu2}. Thus, the Stokes shifts are 0.29 and 0.73 eV, respectively, for Ce_{Lu1} and Ce_{Lu2}, which is consistent with the larger structure relaxation of Ce_{Lu2} than that of Ce_{Lu1} (see Part S2.5 of Supplemental Material [21]). As is well known, large Stokes shifts commonly culminate in very broad luminescence features. In experiment [49], two emission bands of the Ce^{3+} ion at Ce_{Lu1} site are observed, which show the characteristic transition from the $5d$ level to $^2F_{5/2}$ and $^2F_{7/2}$ with peaks at 393 nm (3.16 eV) and 427 nm (2.90 eV), supporting the validity of our approximation on the impact of spin-orbit interaction by adopting $\zeta_{4f} \approx 615\,cm^{-1}$, while it is noted that the Ce^{3+} doublet structure for Ce_{Lu2} is not observed in experiment, and the optical sideband of Ce^{3+} at Lu2 site is much more broad than that at Lu1 site. The experimental excitation and emission energies are 3.48 and 3.16 eV for Ce_{Lu1}, and 3.30 and 2.70 eV for Ce_{Lu2}, and the Stokes shifts are 0.32 and 0.60 eV, respectively, for Ce_{Lu1} and Ce_{Lu2}. Our calculated Stokes shifts of the two sites in the GKS framework are reasonably consistent with experimental observations. However, the calculated excitation and emission energies by utilizing the PBE0 functional (with $\alpha = 0.29$) are about 0.5 eV larger than that in the experiment. The GKS $4f$-$5d$ gaps are substantially overestimated, a smaller hybrid parameter will certainly improve the agreement. As an alternative approach to obtain the optical excitation and emission energies, the HDFT calculated total energies of the ground- and excited states are directly compared. As a result, the excitation and emission energies are calculated to be 4.11 and 3.66 eV for Ce_{Lu1}, and 3.96 and 3.02 eV for Ce_{Lu2} with the impact of spin-orbit interaction involved. And, the Stokes shifts are 0.45 and 0.94 eV, respectively, for Ce_{Lu1} and Ce_{Lu2}. The assessments on optical excitation and emission energies through total energy difference and through GKS energy difference are reasonably consistent.

With the impact of spin-orbit interaction involved, the $4f$-VBM energy difference is also expected to shift downward by about 0.15 eV. As a result, the $4f$-VBM eigenvalue differences are 2.33 and 2.52 eV, respectively, for Ce_{Lu1} and Ce_{Lu2} from our HDFT (PBE0 with $\alpha = 0.29$) calculations, and the corresponding values are 1.36 and 1.53 eV from DFT + $U(U = 4\,eV)$ calculations. As an alternative approach to obtain the $4f$-VBM energy difference, the $4f$ charge-transition levels $\varepsilon(Ce^{4+}/Ce^{3+})$-VBM are calculated to be 1.04 and 1.27 eV (2.95 and 3.20 eV) from GGA-PBE (HDFT-PBE0) calculations, respectively, for Ce_{Lu1} and Ce_{Lu2} with the impact of spin-orbit interaction. It is indicated that our predicted $4f$–VBM values for Ce_{Lu} defects from HDFT-PBE0 calculations are close to the experimental data of 2.6–2.9 eV based on the thermally stimulated luminescence measurements [50]. In the DFT+U method of applying an orbital-dependent potential that adds an extra Coulomb interaction U for the semicore states, the net effect of the added onsite Coulomb interaction is to shift the fully occupied narrow f bands downward by about $U/2$ in energy [51–53]. In this work, the U (4 eV) term is set empirically, resulting in the calculated $4f$-VBM value smaller than the experimental data, which can be attributed to the substantial overestimation of the VBM. HDFT approach certainly improves the agreement of the calculated $4f$-VBM value with the experimental data.

The optical band gap is estimated as the sum of $\varepsilon(Ce^{4+}/Ce^{3+})$–VBM, the zero phonon line energy (E_{zpl}), and the $5d$ thermal ionization energy. E_{zpl} is calculated as the difference between the $4f \rightarrow 5d_1$ excitation energy and the relaxation energy of the $5d_1$ excited state. As listed in Table I, the relaxation energy of the $5d_1$ excited state through direct total-energy comparison is 0.27 and 0.47 eV, and E_{zpl} is 3.84 and 3.49 eV, respectively, for Ce_{Lu1} and Ce_{Lu2}. Considering that the ground-state calculation gives a more reasonable description of the supercell energy than the excited-state calculations, in this work the relaxation energy of the $5d_1$ excited state in the GKS scheme is calculated as the Stokes shift minus the relaxation energy of the $4f$ ground state. As a result, the relaxation energy of $5d_1$ is 0.11 and 0.26 eV, and E_{zpl} is 3.90 and 3.63 eV, respectively, for Ce_{Lu1} and Ce_{Lu2}. The $5d$ thermal ionization energy is calculated as the energy difference between the $5d$ excited state and the ionized state at their corresponding equilibrium atomic configurations. The GKS CBM $- 5d_1$ energy gap at the equilibrium atomic configuration of the excited state is calculated to be 0.56 and 0.67 eV, and the relaxation energy for the ionized Ce^{4+} state is calculated to be 0.65 and 0.56 eV, respectively, for Ce_{Lu1} and Ce_{Lu2}; thus, the $5d$ thermal ionization energy is -0.09 and 0.11 eV, respectively, for Ce_{Lu1} and Ce_{Lu2}. The values of the estimated optical band gap with different calculation schemes (see Table I) are reasonably consistent considering the accuracy of the model and errors in each component, and the average value of 6.8 eV is well consistent with the experimental values of 6.4–6.8 eV [50,54–58]. Actually, a method to determine optimal α and μ in HDFT can be expected not only to produce the correct optical band gap but also to ensure that the defect levels in the gap satisfy the generalized Koopmans' theorem [59,60].

We consider the thermal quenching of the luminescence of Ce^{3+} in LSO due to the $5d$-$4f$ crossing model and/or the $5d$ thermal-ionization model [61]. In the $5d$-$4f$ crossing model, the luminescence center relaxes from the $5d$ state to the $4f$ state via the crossover point of the energy curves. The energy barrier for the crossover point, which is calculated by extrapolating the configuration diagram energy curves from the energies and equilibrium positions of $4f$ and $5d$ states under harmonic approximation, is higher than 2 eV for both the two Ce_{Lu} sites in LSO, while the $5d$ thermal ionization energy in the $5d$ thermal-ionization model is calculated to be quite small (as presented in the previous paragraph), hinting that the thermal quenching mechanism in LSO is thermal ionization from the lowest $5d$ state to the conduction band

TABLE I. Calculated $\varepsilon(\mathrm{Ce}^{4+}/\mathrm{Ce}^{3+})$-VBM, zero phonon line energy (E_{zpl}), $5d$ thermal ionization energy, and the estimated optical band gap of LSO:Ce^{3+} (in eV).

Defect	Scheme	$\varepsilon(\mathrm{Ce}^{4+}/\mathrm{Ce}^{3+})$-VBM	Excitation	Emission	Stokes shift	$4f$ relax	$5d$ relax	E_{zpl}	$5d$ thermal ionization	Optical band gap
$\mathrm{Ce}_{\mathrm{Lu1}}$	GKS energy	2.95	4.01	3.72	0.29		0.11[a]	3.90	−0.09[b]	6.76
	Total energy		4.11	3.66	0.45	0.18	0.27	3.84		6.70
$\mathrm{Ce}_{\mathrm{Lu2}}$	GKS energy	3.20	3.89	3.16	0.73		0.26[a]	3.63	0.11[b]	6.94
	Total energy		3.96	3.02	0.94	0.47	0.47	3.49		6.80

[a] The $5d$ relaxation energy is calculated as the Stokes shift minus the relaxation energy of the $4f$ ground state.

[b] The $5d$ thermal ionization energy is calculated as the energy difference between the $5d$ excited state and the ionized state at their corresponding equilibrium atomic configurations, i.e., the GKS CBM $-$ $5d_1$ energy gap at the equilibrium atomic configuration of the excited state minus the relaxation energy for the ionized Ce^{4+} state.

(CB) rather than a multiphonon radiationless transition to the $4f$ ground state, well in agreement with the experimental photoconductivity measurements [62]. The configuration coordinate diagrams for the photon emission of the two $\mathrm{Ce}_{\mathrm{Lu}}$ sites are plotted in Figs. 5(c) and 5(d).

Actually, by examining the orbitals at the equilibrium atomic configuration of the Ce^{4+}-doped supercell, the lowest $5d$ orbital is higher than the CBM both for the two $\mathrm{Ce}_{\mathrm{Lu}}$ sites; thus, the stable Ce^{4+} center efficiently competes with any electron traps for immediate capture of electrons from the CB, which fits the experimentally proposed scintillation model of stable Ce^{4+} in which Ce^{4+} first captures an electron from the CB, then the center (at an intermediate Ce^{3+} excited state) radiates, and finally returns to the initial state by capturing a hole [4,9,63–66]. However, the stable Ce^{3+} center first needs to capture the hole from the valence band, which is temporarily converted into Ce^{4+}, then captures an electron from the CB and becomes excited [66]. In brief, the Ce^{4+} ions contribute to the fastest part of the scintillation response. Thus, Ca codoping leads to the emergence of some Ce^{4+} ions and shortens the scintillation decay time of LSO:Ce.

As the total concentration of the dopant Ce is generally larger than that of the intrinsic V_{O} defects in LSO:Ce, and it is indicated from the binding energies that the $\mathrm{Ce}_{\mathrm{Lu}}$ dopants tend to combine the V_{O} defects, therefore it is reasonable to assume that a large fraction of V_{O} defects has a Ce atom in their proximity. Moreover, it is noted that the V_{O} defects exhibit substantial structural relaxation between different charge states in LSO; these defects thus possibly play important roles in the charge transfer from $\mathrm{Ce}_{\mathrm{Lu}}$. In view of the predominance of the $\mathrm{Ce}_{\mathrm{Lu1}}$ site over the $\mathrm{Ce}_{\mathrm{Lu2}}$ site, we consider in detail the possible nonradiative process of $\mathrm{Ce}_{\mathrm{Lu1}}$ via its spatial-correlated doubly charged $V_{\mathrm{O1}}^{\cdot\cdot}$ or singly charged $V_{\mathrm{O1}}^{\cdot}$. As schematically illustrated in Figs. 5(a) and 5(b), after the neutral $\mathrm{Ce}_{\mathrm{Lu1}}^{\times}$ defect is excited, the $5d$ electron would immediately be transferred from $(\mathrm{Ce}_{\mathrm{Lu1}}^{\times})^{*}$ to $V_{\mathrm{O1}}^{\cdot\cdot}$ (or $V_{\mathrm{O1}}^{\cdot}$), leading to a singly charged $\mathrm{Ce}_{\mathrm{Lu1}}^{\cdot}$ and a singly charged $V_{\mathrm{O1}}^{\cdot}$ (or a neutral $V_{\mathrm{O1}}^{\times}$). The subsequent relaxation for the $\mathrm{Ce}_{\mathrm{Lu1}}^{\cdot} + V_{\mathrm{O1}}^{\cdot}$ state (or $\mathrm{Ce}_{\mathrm{Lu1}}^{\cdot} + V_{\mathrm{O1}}^{\times}$ state) decreases the energy even by 2.14 eV (or 2.17 eV) via coupling to lattice vibrations. At this point, the system is trapped in a low-energy state in its equilibrium configuration, and the energy barrier to escape from

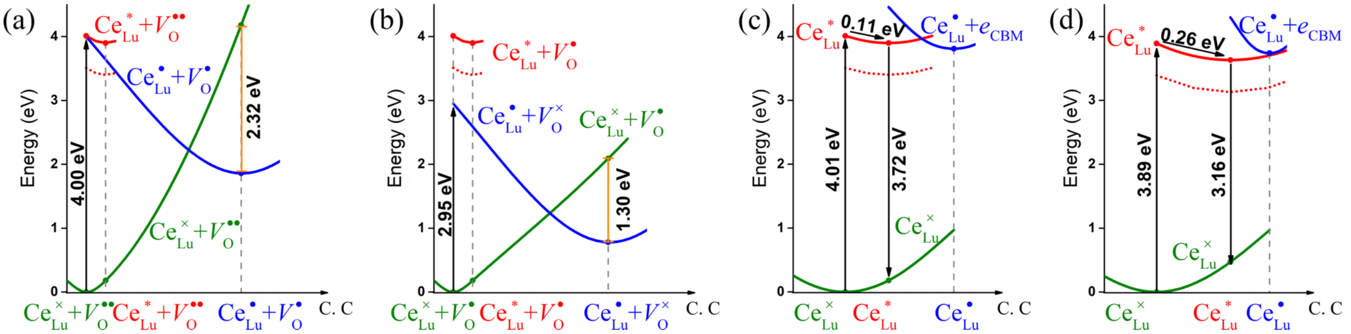

FIG. 5. Configuration coordinate diagrams for the nonradiative decay of $\mathrm{Ce}_{\mathrm{Lu1}}$ via $V_{\mathrm{O1}}^{\cdot\cdot}$ (a) and via $V_{\mathrm{O1}}^{\cdot}$ (b), and for the photon emission of $\mathrm{Ce}_{\mathrm{Lu1}}$ (c) and $\mathrm{Ce}_{\mathrm{Lu2}}$ (d). Solid lines plot the total energy for each indicated state, and the configurations on the abscissa refer to the equilibrium configuration of the respective state. Red dotted lines are intended as an aid to the eye on the aligned energy of the excited $(\mathrm{Ce}^{3+})^{*}$ state by referring to the measurements. With Ca codoped, the formation of $\mathrm{Ca}_{\mathrm{Lu}}$-$V_{\mathrm{O}}$ causes the dissociation of the originally spatial-correlated V_{O} and $\mathrm{Ce}_{\mathrm{Lu}}$; thus, the nonradiative decay of Ce via V_{O} would be effectively suppressed, leading to the improvement in the photon emission of Ce.

this configuration back to $\mathrm{Ce}_{\mathrm{Lu1}}^{\times}$ in combination with $V_{\mathrm{O1}}^{\cdot\cdot}$ (or $V_{\mathrm{O1}}^{\cdot}$) is 2.32 (or 1.30 eV), as the orange lines indicate in Fig. 5. With Ca codoped, the formation of $\mathrm{Ca}_{\mathrm{Lu}}$-$V_{\mathrm{O}}$ complex defects causes the dissociation of the originally spatial-correlated V_{O} and $\mathrm{Ce}_{\mathrm{Lu}}$; thus, the nonradiative decay of Ce via its surrounding positively charged V_{O} would be effectively suppressed, leading to the improvement in the photon emission of Ce, as indicated in Figs. 5(c) and 5(d) in the GKS framework. Therefore, the light yield of LSO:Ce is substantially enhanced by Ca codoping.

IV. FUTURE PERSPECTIVES

On the basis of the discussions of LSO:Ce, Ca, the effect of Li codoping on the scintillation properties of LSO:Ce can be interpreted by referring to previous related studies [67,68]; for the detailed analysis see Part S3.1 of Supplemental Material [21]. We further give suggestions for scintillator property tuning from choices of the host band gap [69], the characteristics of the dopant ions and the defect engineering such as annealing [44], and codoping. Simultaneously, as a powerful approach for assessing the properties, theoretical simulation can be used to provide guidance for designing and optimizing functional materials. Detailed suggestions to design and optimize related materials are provided in Part S3.2 of Supplemental Material [21].

V. CONCLUSION

To summarize, a comprehensive understanding on the effect of Ca codoping on both the scintillation light yield and decay time of LSO:Ce is achieved based on first-principles calculations. It is concluded that the enhancement of light yield and the shortening of decay time are attributed to the suppression of the charge transfer from Ce to the spatial-correlated V_{O} and the formation of stable Ce^{4+} ions, respectively. Specifically, the formation of $\mathrm{Ca}_{\mathrm{Lu}}$-$V_{\mathrm{O}}$ causes the dissociation of $\mathrm{Ce}_{\mathrm{Lu}}$-$V_{\mathrm{O}}$ complex defects; the nonradiative decay of Ce is therefore effectively suppressed, leading to the improvement in the photon emission of Ce. Moreover, the downward shift of the Fermi level with the codoping of Ca causes the observation of stable Ce^{4+} ions, and the combination with Ca decreases the electron trap depth of V_{O}; both the two processes contribute to the faster trapping/detrapping rates, leading to scintillation decay-time shortening of LSO:Ce. The obtained mechanism can be applied not only to understand the effect of Li codoping on the properties of LSO:Ce, but also to design and optimize related materials.

ACKNOWLEDGMENTS

We thank Professor Chang-Kui Duan (University of Science and Technology of China) for valuable discussions and helpful suggestions. Numerical calculations in this paper were performed on the supercomputing system in the Supercomputing Center of University of Science and Technology of China. This work was supported by the Doctoral Scientific Research Start-up Foundation from Henan University of Technology (Grant No. 2019BS036).

---

[1] C. L. Melcher and J. S. Schweitzer, IEEE Trans. Nucl. Sci. **39**, 502 (1992).

[2] Y. Wu, M. Tian, J. Peng, M. Koschan, I. Greeley, C. Foster, and C. L. Melcher, Phys. Status Solidi RRL **13**, 1800472 (2019).

[3] K. Yang, C. L. Melcher, P. D. Rack, and L. A. Eriksson, IEEE Trans. Nucl. Sci. **56**, 2960 (2009).

[4] Y. Wu, M. Koschan, Q. Li, I. Greeley, and C. L. Melcher, J. Cryst. Growth **498**, 362 (2018).

[5] Y. Wu, J. Peng, D. Rutstrom, M. Koschan, C. Foster, and C. L. Melcher, ACS Appl. Mater. Interfaces **11**, 8194 (2019).

[6] Y. D. Zavartsev, S. A. Koutovoi, and A. I. Zagumennyi, J. Cryst. Growth **275**, e2167 (2005).

[7] A. A. Masalov, O. G. Vyagin, I. I. Ganina, Y. V. Malyukin, I. M. Zenya, and N. G. Starzhinskii, Tech. Phys. Lett. **35**, 154 (2009).

[8] N. G. Starzhinskiy, O. T. Sidletskiy, G. Tamulaitis, K. A. Katrunov, I. M. Zenya, Y. V. Malyukin, O. V. Viagin, A. A. Masalov, and I. A. Rybalko, IEEE Trans. Nucl. Sci. **60**, 1427 (2013).

[9] S. Blahuta, A. Bessière, B. Viana, P. Dorenbos, and V. Ouspenski, IEEE Trans. Nucl. Sci. **60**, 3134 (2013).

[10] A. Alkauskas, M. D. McCluskey, and C. G. Van de Walle, J. Appl. Phys. **119**, 181101 (2016).

[11] K. Hoang and M. D. Johannes, J. Phys.: Condens. Matter **30**, 293001 (2018).

[12] P. Dorenbos, C. W. E. Van Eijk, A. J. J. Bos, and C. L. Melcher, J. Phys.: Condens. Matter **6**, 4167 (1994).

[13] J. P. Perdew, W. Yang, K. Burke, Z. Yang, E. K. U. Gross, M. Scheffler, G. E. Scuseria, T. M. Henderson, I. Y. Zhang, A. Ruzsinszky, H. Peng, J. Sun, E. Trushin, and A. Görling, Proc. Natl. Acad. Sci. **114**, 2801 (2017).

[14] J. P. Perdew, K. Burke, and M. Ernzerhof, Phys. Rev. Lett. **77**, 3865 (1996).

[15] G. Kresse and J. Hafner, Phys. Rev. B **47**, 558 (1993).

[16] G. Kresse and J. Furthmüller, Phys. Rev. B **54**, 11169 (1996).

[17] G. Kresse and J. Furthmüller, Comput. Mater. Sci. **6**, 15 (1996).

[18] G. Kresse and D. Joubert, Phys. Rev. B **59**, 1758 (1999).

[19] P. E. Blöchl, Phys. Rev. B **50**, 17953 (1994).

[20] T. Gustafsson, M. Klintenberg, S. E. Derenzo, M. J. Weber, and J. O. Thomas, Acta Crystallogr., Sect. C **57**, 668 (2001).

[21] See Supplemental Material at http://link.aps.org/supplemental/10.1103/PhysRevB.107.085149 for additional computational details on atomic coordinates and geometric parameters of $\mathrm{Lu_2SiO_5}$, ranges of chemical potentials, and corrections; complementary results on relative formation energy of the isomeric V_{O}, V_{Lu}, I_{O}, $\mathrm{Ce}_{\mathrm{Lu}}$, and $\mathrm{Ca}_{\mathrm{Lu}}$ defects, relative formation energy of the isomeric V_{O}-$\mathrm{Ce}_{\mathrm{Lu}}$ and V_{O}-$\mathrm{Ca}_{\mathrm{Lu}}$ complex defects, binding energy of the dominant V_{O}-involved complex defects, charge transition level (CTL) of defects, and structure relaxation of $\mathrm{Ce}_{\mathrm{Lu1}}$ and $\mathrm{Ce}_{\mathrm{Lu2}}$; detailed future perspectives on effect of Li

codoping on scintillation properties of LSO:Ce and suggestions for scintillator property tuning.
[22] V. Fiorentini and A. Baldereschi, Phys. Rev. B **51**, 17196 (1995).
[23] M. A. L. Marques, J. Vidal, M. J. T. Oliveira, L. Reining, and S. Botti, Phys. Rev. B **83**, 035119 (2011).
[24] F. Viñes, O. Lamiel-García, K. Chul Ko, J. Yong Lee, and F. Illas, J. Comput. Chem. **38**, 781 (2017).
[25] M. Kitaura, S. Tanaka, and M. Itoh, J. Lumin. **158**, 226 (2015).
[26] C. Freysoldt, B. Grabowski, T. Hickel, J. Neugebauer, G. Kresse, A. Janotti, and C. G. Van de Walle, Rev. Mod. Phys. **86**, 253 (2014).
[27] C. H. Rim, C. H. Jang, K. H. Kim, C. Ryu, and C. J. Yu, Phys. Chem. Chem. Phys. **24**, 22736 (2022).
[28] C. Freysoldt, J. Neugebauer, and C. G. Van de Walle, Phys. Rev. Lett. **102**, 016402 (2009).
[29] Y. Kumagai and F. Oba, Phys. Rev. B **89**, 195205 (2014).
[30] S. Lany and A. Zunger, Phys. Rev. B **78**, 235104 (2008).
[31] G. Makov and M. C. Payne, Phys. Rev. B **51**, 4014 (1995).
[32] M. Leslie and N. J. Gillan, J. Phys. C: Solid State Phys. **18**, 973 (1985).
[33] T. R. Durrant, S. T. Murphy, M. B. Watkins, and A. L. Shluger, J. Chem. Phys. **149**, 024103 (2018).
[34] Y. Kumagai, L. A. Burton, A. Walsh, and F. Oba, Phys. Rev. Appl. **6**, 014009 (2016).
[35] Y. Jia, A. Miglio, M. Mikami, and X. Gonze, Phys. Rev. Mater. **2**, 125202 (2018).
[36] G. Ren, L. Qin, H. Li, and S. Lu, Cryst. Res. Technol. **41**, 163 (2006).
[37] A. Lempicki, C. Brecher, H. Lingertat, S. R. Miller, J. Glodo, and V. K. Sarin, IEEE Trans. Nucl. Sci. **55**, 1148 (2008).
[38] R. D. Shannon, Acta Crystallogr., Sect. A **32**, 751 (1976).
[39] K. Yang, C. L. Melcher, M. A. Koschan, and M. Zhuravleva, IEEE Trans. Nucl. Sci. **58**, 1394 (2011).
[40] L. Pidol, O. Guillot-Noël, A. Kahn-Harari, B. Viana, D. Pelenc, and D. Gourier, J. Phys. Chem. Solids **67**, 643 (2006).
[41] A. Y. Kuznetsov, A. B. Sobolev, A. N. Varaksin, and O. A. Keda, Phys. Status Solidi B **204**, 701 (1997).
[42] C. L. Melcher, S. Friedrich, S. P. Cramer, M. A. Spurrier, P. Szupryczynski, and R. Nutt, IEEE Trans. Nucl. Sci. **52**, 1809 (2005).
[43] W. Zhou, J. Vavro, N. M. Nemes, J. E. Fischer, F. Borondics, K. Kamaras, and D. B. Tanner, Phys. Rev. B **71**, 205423 (2005).
[44] D. Ding, H. Feng, G. Ren, M. Nikl, L. Qin, S. Pan, and F. Yang, IEEE Trans. Nucl. Sci. **57**, 1272 (2010).
[45] C. Linderalv, A. Lindman, and P. Erhart, J. Phys. Chem. Lett. **9**, 222 (2018).
[46] A. Gali, E. Janzén, P. Deák, G. Kresse, and E. Kaxiras, Phys. Rev. Lett. **103**, 186404 (2009).
[47] J. Cai, W. Jing, J. Cheng, Y. Zhang, Y. Chen, M. Yin, Y. Y. Yeung, and C. K. Duan, Phys. Rev. B **99**, 125107 (2019).
[48] L. van Pieterson, M. F. Reid, R. T. Wegh, S. Soverna, and A. Meijerink, Phys. Rev. B **65**, 045113 (2002).
[49] H. Suzuki and T. A. Tombrello, IEEE Trans. Nucl. Sci. **40**, 380 (1993).
[50] A. Vedda, M. Nikl, M. Fasoli, E. Mihokova, J. Pejchal, M. Dusek, G. Ren, C. R. Stanek, K. J. McClellan, and D. D. Byler, Phys. Rev. B **78**, 195123 (2008).
[51] V. I. Anisimov, F. Aryasetiawan, and A. I. Lichtenstein, J. Phys.: Condens. Matter **9**, 767 (1997).
[52] S. L. Dudarev, G. A. Botton, S. Y. Savrasov, C. J. Humphreys, and A. P. Sutton, Phys. Rev. B **57**, 1505 (1998).
[53] E. Finazzi, C. Di Valentin, G. Pacchioni, and A. Selloni, J. Chem. Phys. **129**, 154113 (2008).
[54] D. W. Cooke, B. L. Bennett, K. J. McClellan, J. M. Roper, M. T. Whittaker, and A. M. Portis, Phys. Rev. B **61**, 11973 (2000).
[55] M. Kobayashi, M. Ishii, and C. L. Melcher, Nucl. Instrum. Methods Phys. Res., Sect. A **335**, 509 (1993).
[56] I. A. Kamenskikh, V. V. Mikhailin, I. H. Munro, D. Y. Petrovykh, D. A. Shaw, P. A. Studenikin, A. N. Vasil'ev, I. A. Zagumennyi, and Y. D. Zavartsev, Radiat. Eff. Defect. Solids **135**, 391 (1995).
[57] A. Lempicki and J. Glodo, Nucl. Instrum. Methods Phys. Res., Sect. A **416**, 333 (1998).
[58] L. Ning, L. Lin, L. Li, C. Wu, C. K. Duan, Y. Zhang, and L. Seijo, J. Mater. Chem. **22**, 13723 (2012).
[59] P. Deák, Q. Duy Ho, F. Seemann, B. Aradi, M. Lorke, and T. Frauenheim, Phys. Rev. B **95**, 075208 (2017).
[60] S. Lany and A. Zunger, Phys. Rev. B **80**, 085202 (2009).
[61] S. Poncé, Y. Jia, M. Giantomassi, M. Mikami, and X. Gonze, J. Phys. Chem. C **120**, 4040 (2016).
[62] E. Van der Kolk, S. A. Basun, G. F. Imbusch, and W. M. Yen, Appl. Phys. Lett. **83**, 1740 (2003).
[63] S. Liu, X. Feng, Z. Zhou, M. Nikl, Y. Shi, and Y. Pan, Phys. Status Solidi RRL **8**, 105 (2014).
[64] M. Nikl, K. Kamada, V. Babin, J. Pejchal, K. Pilarova, E. Mihokova, A. Beitlerova, K. Bartosiewicz, S. Kurosawa, and A. Yoshikawa, Cryst. Growth Des. **14**, 4827 (2014).
[65] Y. Wu, F. Meng, Q. Li, M. Koschan, and C. L. Melcher, Phys. Rev. Appl. **2**, 044009 (2014).
[66] M. Nikl, V. Babin, J. Pejchal, V. V. Laguta, M. Bruyi, J. A. Mares, K. Kamada, S. Kurosawa, A. Yoshikawa, D. Panek, T. Parkman, P. Bruza, K. Mann, and M. Müller, IEEE Trans. Nucl. Sci. **63**, 433 (2016).
[67] L. Jia, J. Zhu, Y. Teng, and M. Gu, Mater. Lett. **228**, 372 (2018).
[68] M. V. Derdzyan, K. L. Hovhannesyan, A. V. Yeganyan, R. V. Sargsyan, A. Novikov, A. G. Petrosyan, and C. Dujardin, CrystEngComm **20**, 1520 (2018).
[69] M. Nikl and A. Yoshikawa, Adv. Opt. Mater. **3**, 463 (2015).